Accretion Disk Evolution with Wind Infall II. Results of 3D Hydrodynamical Simulations with an Illustrative Application to Sgr A*

Robert Coker[1]
Department of Physics, University of Arizona, Tucson, AZ 85721 (rfc@physics.arizona.edu)

Fulvio Melia[2]
Department of Physics & Steward Observatory, University of Arizona, Tucson, AZ 85721 (melia@as.arizona.edu)

Heino Falcke
Max-Planck-Institut für Radioastronomie, Auf dem Hügel 69, D-53121, Bonn, Germany. (hfalcke@mpifr-bonn.mpg.de)
Steward Observatory, University of Arizona, Tucson, AZ 85721

ABSTRACT

In the first paper of this series, using analytic tools, we examined how the evolution and structure of a massive accretion disk may be influenced significantly by the deposition of mass and angular momentum by an infalling Bondi-Hoyle wind. Such a mass influx impacts the long-term behavior of the disk by providing additional sources of viscosity and heating. In this paper, we make a significant improvement over this earlier work by incorporating the results of 3D hydrodynamical simulations of the large scale accretion from an ambient medium into the disk evolution equations developed previously. We discuss in detail two models, one with the axis of the disk parallel to, and the second with the axis oriented perpendicular to the large scale Bondi-Hoyle flow. We find that the mass inflow rate onto the disk within logarithmic annuli is roughly constant with radius and that the impacting wind carries much less specific angular momentum than Keplerian. We also find, in general, that the infrared spectrum of a wind-fed disk system is steeper than that of a Shakura-Sunyaev configuration, due mainly to the dissipation of the wind's kinetic energy at the disk's surface. In applying our results to the Galactic Center black hole candidate, Sgr A*, accreting from nearby stellar winds, we demonstrate that a high wind inflow rate of order $10^{-4} M_\odot$ per year cannot be incorporated into a fossil disk without a significant dissipation of kinetic energy at all radii. Such a high dissipation would violate current infrared and near-infrared limits on the observed spectrum of Sgr A*.

Subject headings: accretion, accretion disks, Bondi-Hoyle—black hole physics—Galaxy: center—Galaxy: Sgr A*

---

[1]NASA GSRP Fellow.

[2]Presidential Young Investigator.

1. Introduction

In this paper, we will continue our study of the effects on massive accretion disk evolution due to the continued infall from Bondi-Hoyle accretion. This problem is of general interest to systems in which the mass influx is not planar at the disk's outer edge, but rather originates from a 3-dimensional distribution of wind sources. An example is the formation and evolution of a protostellar disk, or a disk embedded within a cluster of stellar wind sources, such as may be the case for the black hole candidate Sgr A* at the Galactic Center. In our application, 3D hydrodynamic simulations of the Bondi-Hoyle infall are used to provide more realistic profiles of the accreted mass, temperature, and specific angular momentum as functions of radius. These profiles are incorporated into the one-dimensional equations for the temporal evolution of accretion disks with wind infall developed in Falcke & Melia 1997 (Paper I).

1.1. Galactic Center Bondi-Hoyle Accretion

Spectral and kinematic studies suggest that the powerful nonthermal radio source Sgr A*, located at the center of the Milky Way, is a supermassive compact object with a mass $\sim 2-3\times10^6\,M_\odot$. This inference is based on the large proper motion of nearby stars (Haller, et al. 1995; Eckart & Genzel 1997; Genzel, Eckart, Ott, & Eisenhauer 1997), the spectrum of Sgr A* (e.g., Melia, Jokipii, & Narayanan 1992), its low proper motion ($\lesssim 20\,\mathrm{km\,s^{-1}}$; Backer 1996), and its unique location (Lacy, Achtermann, & Serabyn 1991). Measurements of high outflow velocities associated with sources near Sgr A* (Krabbe, et al. 1991; Geballe, et al. 1991), as well as emission line (Gatley, et al. 1986; Hall, Kleinmann, & Scoville 1982; Allen, Hyland, & Hillier 1990; Geballe, et al. 1991) and radio continuum observations (Yusef-Zadeh & Melia 1991), provide clear evidence of a hypersonic wind pervading the inner parsec of the Galaxy. This Mach $= 10-30$ wind has a velocity $v_w = 500-1000\ \mathrm{km\,s^{-1}}$, a number density $n_w = 10^{3-4}\ \mathrm{cm^{-3}}$, and a total mass outflow rate $\dot{M}_w = 3-4\times10^{-3}\ M_\odot\ \mathrm{yr^{-1}}$.

Sgr A*'s radiative characteristics, should be directly or indirectly due to its accretion of this wind. In the classical Bondi-Hoyle (BH) scenario (Bondi & Hoyle 1944), the mass accretion rate for a uniform hypersonic flow is

$$\dot{M}_{BH} = \pi {R_A}^2 m_H n_w v_w, \tag{1}$$

in terms of the accretion radius $R_A \equiv 2GM/{v_w}^2$. At the Galactic Center, using $M \sim 10^6\,M_\odot$, $n_w \sim 5.5\times10^3\,\mathrm{cm^{-3}}$, and $v_w \sim 700\,\mathrm{km\,s^{-1}}$, we would therefore expect an accretion rate $\dot{M}_{BH} \sim 6\times10^{21}\,\mathrm{g\,s^{-1}}$ onto the black hole, with a capture radius $R_A \sim 0.02\,\mathrm{pc}$. Since this accretion rate is sub-Eddington for a million solar mass object, the accreting gas is mostly unimpeded by the escaping radiation field and is thus essentially in hydrodynamic free-fall starting at R_A. Our initial numerical simulations of this process, assuming a highly simplistic uniform flow past a $1\times10^6\,M_\odot$ point mass (Ruffert & Melia 1994; Coker & Melia 1996) have verified these expectations.

Whether or not this accretion is mediated via an accretion disk or it constitutes a more or less quasi-spherical infall depends critically on the specific angular momentum carried by the captured gas. Therefore, it is not always clear whether disk or quasi-spherical accretion dominates or if both are present. However, in the case of Sgr A*, if the surrounding winds are relatively uniform, the fluctuations in the accreted specific angular momentum are sufficiently small that only a small accretion disk, less than about $\sim 50\ R_s$ in radius (where $R_s \equiv 2GM/c^2$ is the Schwarzschild radius) is then expected to form (Ruffert & Melia 1994; Coker & Melia 1996). However, non-uniformities in the ambient medium, due to individual stellar wind sources, could result in a greater specific angular momentum being accreted with the captured material (Coker & Melia 1997), and hence account for a larger circularization radius (but still $\lesssim 5000 R_s$) and presumably a larger and brighter accretion disk. Another way of saying this is that the infalling gas from a non-uniform medium may retain a larger Keplerian energy that must be dissipated (or, possibly, advected) as it drifts inwards towards the black hole.

1.2. Massive Accretion Disk Models

Although the broadband radiative emission from Sgr A* may be produced either in the quasi-spherical accretion portion of the inflow (Melia 1994) or by a radio jet (Falcke, Mannheim, & Biermann 1993, Falcke & Biermann 1999), the low total luminosity of Sgr A* ($\lesssim$ a few $10^5 L_\odot$; Zylka et al. 1995) seems to point to either a much lower accretion rate ($\ll 10^{21}\,\mathrm{g\,s^{-1}}$), if one assumes a conversion efficiency of 10% rest mass energy into radiation, or a low conversion efficiency ($\lesssim 10^{-5}$). Sgr A* appears to be the ideal case for applying the concept of *any* large, stable accretion disk fed by quasi-spherical accretion since the disk acts as a resevoir for the infalling plasma, thereby decreasing the expected conversion efficiency and luminosity.

An α-disk model with an accretion rate implied by Equation (1) is not consistent with the observed infrared faintness of Sgr A* (Melia 1994). Thus, if a disk is present in this source, it must either be very faint due to its "fossilized" nature, or it must be advection dominated, such that most of its dissipated energy is swept through the event horizon before it can be radiated away. The disk evolution equations derived in Paper I (Falcke & Melia 1997) apply to the former case. The structure of advection dominated disks, on the other hand, depends on both the state variables and their gradients, so their evolution must be handled globally, not locally. Thus, although we discuss both in this paper, our quantitative results for the impact of a wind infall on the disk's evolution, apply primarily to the former.

1.2.1. A Fossil Disk

It has been suggested (Falcke & Heinrich 1994, Falcke 1996) that Sgr A* might be surrounded by a large, slowly accreting, fossil disk, perhaps formed from the remnants of a tidally-disrupted star that ventured too close to the black hole. Depending on the strength of such a disruption, as much as half of the stellar mass may be left as a remnant surrounding the black hole (Khokhlov & Melia 1996 and references cited therein). This remnant may, under some circumstances, form a relatively cold disk that evolves without a substantial mass infusion at its outer edge. A fossil disk may also exist as the remnant of a phase of higher activity in the past (Falcke & Heinrich 1994). In both cases, one expects that the large-scale Bondi-Hoyle inflow must be captured and incorporated into the fossil disk. The resulting observational signature will then depend strongly on the ratio of wind to disk accretion rates, the viscosity in the disk, the specific angular momentum of the infalling matter and the time scales involved. For example, the fossil disk could remain faint for long periods of time if the inflowing gas has a large specific angular momentum, for it would then get absorbed onto the plane at large radii where the dissipation rate is relatively small (Paper I).

1.2.2. An Advection Dominated Disk

The disk in sources such as Sgr A* may also be faint because it is advection dominated (Abramowicz, et al. 1995; Narayan, Yi, & Mahadevan 1995). In this case, the accretion is highly advective, decreasing the expected luminosity by up to an order of magnitude or more. This occurs because a large fraction (90% or more) of the dissipated gravitational energy flux is carried inwards through the event horizon by the disk plasma. This model requires a small mass accretion rate ($\lesssim 10^{-5}$ $M_\odot$ yr^{-1}) compared to the value indicated by Equation (1), a large α ($\gtrsim 0.1$), and a large disk scale size ($\sim 0.02\,\mathrm{pc}$) in order to produce the required low efficiency. Some of the results discussed in this paper, particularly the kinetic energy dissipated and radiated as the infalling wind impacts the plane, will be valid in a qualitative sense for this type of disk just as they are for a fossilized structure. We caution, however, that the evolution of an advection dominated disk cannot be described adequately with the equations presented below, and so quantitative conclusions regarding the impact of a wind infall must in this case await future work.

1.3. Scope and Outline of the Paper

In Section 2 we summarize the pertinent results of Paper I and discuss how the numerical results will be incorporated into the model. In Section 3 we present some of the details and results of the hydrodynamical simulations. The implications for the Galactic Center are discussed in Section 4. We provide a summary and describe further applications of our model in Section 5.

2. The Disk Equations with Infall

The structure of the infalling wind is determined by the hydrodynamical simulations (see Section 3). This wind impacts the disk, resulting in a total dissipation rate (for each side of the disk):

$$D(r,t) = D_{\mathrm{d}} + D_{\mathrm{w}}, \tag{2}$$

where D_{d} is the internal energy dissipation caused by turbulent viscosity and differential rotation of the disk and is given by:

$$D_{\mathrm{d}} = \frac{1}{2}\,\nu\Sigma\left(r\frac{\partial\omega}{\partial r}\right)^2, \tag{3}$$

and D_{w} is the dissipation rate due to the infalling wind's kinetic energy relative to the disk being converted into thermal energy:

$$D_{\mathrm{w}} = \frac{1}{2}\dot{\Sigma}_{\mathrm{w}}{v_w}^2, \tag{4}$$

where v_w is the wind velocity relative to the disk's motion and, assuming $v_r^d \ll v_r$ (see Eq. 14), is given by:

$$v_w = r^2\omega^2(1-\xi)^2 + {v_z}^2 + {v_r}^2. \tag{5}$$

In the preceding equations, Σ is the disk's surface density, r is the radius, $\dot{\Sigma}_{\mathrm{w}}$ is the mass infall onto the disk per unit area and time, ω is the disk's rotational frequency, $\partial\omega/\partial r$ is the radial derivative of ω, v_z and v_r are the z- and r-component, respectively, of the wind's velocity just before it impacts the disk, ν is the internal disk viscosity, and ξ is the ratio of the impacting wind's azimuthal velocity to its Keplerian value.

It is then assumed that the total observed energy flux is the sum of the energy dissipated in the disk and the energy dissipated by the impact of the wind on the surface of the disk so that we have

$$F_{\rm tot} = \sigma T_{\rm eff}(r,t)^4 = D(r,t), \tag{6}$$

where σ is the Stefan-Boltzmann constant. This expression assumes that the disk is optically thick. To obtain the spectrum, we use a sum of blackbodies at the local effective temperature $T_{\rm eff}(r,t)$.

¿From the hydrodynamical simulations, we get spatial and temporal profiles for ξ, $\dot{\Sigma}_{\rm w}$, and v_w, while the assumption of a Keplerian disk provides ω and $\partial\omega/\partial r$. This leaves Σ and ν to be determined. For Σ, we use the well-known differential equation for the time evolution of the surface density of an accretion disk, but now including the effects of wind infall:

$$\frac{\partial\Sigma}{\partial t} = \frac{3}{r}\frac{\partial}{\partial r}\left[r^{1/2}\frac{\partial}{\partial r}\left(\nu\Sigma r^{1/2}\right) + \frac{2}{3}(1-\xi)r^2\dot{\Sigma}_{\rm w}\right] + \dot{\Sigma}_{\rm w}\,. \tag{7}$$

For ν, we adopt the standard Shakura-Sunyaev α-prescription so that:

$$\nu = \alpha c_{\rm s} z_0\ , \tag{8}$$

where α is the dimensionaless viscosity parameter, $c_{\rm s}$ is the local sound speed in the midplane of the disk given by

$$c_{\rm s} = \sqrt{\frac{\gamma k_{\rm b} T(0)}{\mu m_{\rm p}}}, \tag{9}$$

and z_0 is the scale height of a gas-pressure dominated configuration, given by

$$z_0 = \frac{c_{\rm s}}{\omega}\left\{\left[\left(\frac{1}{2}\frac{\dot{\Sigma}_{\rm w}}{\Sigma\omega}\frac{v_{\rm z}}{c_{\rm s}}\right)^2 + 1\right]^{1/2} - \frac{1}{2}\frac{\dot{\Sigma}_{\rm w}}{\Sigma\omega}\frac{v_{\rm z}}{c_{\rm s}}\right\}. \tag{10}$$

As discussed in Paper I, the temperature, $T(0)$, at the midplane of the disk is given by

$$T(0)^4 = \frac{1}{\sigma}\left[\left(\frac{3\kappa\Sigma}{4} + 1\right)D_{\rm d} + D_{\rm w}\right]. \tag{11}$$

We assume the opacity, κ, is due to free-free scattering and is given by

$$\kappa = 6.6\times10^{22}\ {\rm cm^2\ g^{-1}}\left(\frac{\rho}{1\ {\rm g\,cm^{-3}}}\right)\left(\frac{T}{1\ {\rm K}}\right)^{-7/2}. \tag{12}$$

Thus, for a given initial set up, one starts with an estimate of $T(0)$ in order to obtain $c_{\rm s}$, ν, and $D(r)$. Using Equation 11, a new temperature estimate is made; the system rapidly converges. Since $c_{\rm s}$ changes slowly, the sound speed from the previous time step can be used in a Runge-Kutta algorithm with adaptive step size for the time evolution of $\Sigma(r,t)$.

It is also useful to know the rate, $\dot{M}$, with which the mass is flowing radially through the disk:

$$\dot{M} = 2\pi r v_r^d \Sigma\ , \tag{13}$$

where v_r^d is the radial velocity of gas in the disk and is given by the expression

$$v_r^d = -\frac{3}{r\Sigma}\left[r^{1/2}\frac{\partial}{\partial r}\left(\nu\Sigma r^{1/2}\right) + \frac{2}{3}(1-\xi)r^2\dot{\Sigma}_{\rm w}\right]. \tag{14}$$

3. The Hydrodynamical Simulations

3.1. The Code

We use a modified version of the 3D hydrodynamics code ZEUS, a general purpose code for MHD fluids developed at NCSA (Stone & Norman 1992; Norman 1994). The code uses Eulerian finite differencing with the following relevant characteristics: fully explicit in time; operator and directional splitting of the hydrodynamical variables; fully staggered grid; second-order (van Leer) upwinded, monotonic interpolation for advection; consistent advection to evolve internal energy and momenta; and explicit solution of internal energy. More details can be found in the references.

We concentrate primarily on the hydrodynamical aspects of the infall and therefore exclude the effects of magnetic heating and radiative cooling, even though bremsstrahlung and, especially, magnetic bremsstrahlung emission may become significant at smaller radii. Thus, the gas is assumed to be an adiabatic, polytropic gas with $\gamma = 5/3$. The quantitative results presented here may be altered with the inclusion of more of the relevant physics (heating and cooling, magnetic fields, and individual wind sources); this may be addressed in future work.

3.2. The Setup

The first step is to run a large scale simulation, with a volume of solution $16R_A$ or $\sim$0.28 pc on a side; the results are used as boundary conditions for subsequent small scale simulations which are 0.001 pc on a side. The size of the large simulation was chosen so as to maximize spatial resolution while minimizing boundary effects. The size of the small simulation was chosen to again maximize resolution while having its outer boundary as close as possible to the large simulation's inner boundary. The large scale run lasts 1500 years to ensure that equilibrium is reached and the last 100 years are used for the 100 year long small scale simulations. A single simulation, combinding the large and small scale, would be ideal, but the high spatial resolution required in the central region, when combined with the need to satisfy the Courant condition, makes such a calculation computationally prohibitive at present.

Since we are primarily interested in a basic understanding of the disk evolution due to the infalling wind, we use a simple hydrodynamical setup. That is, we assume the wind is uniform and enters the volume of solution from the +z directon; all other faces of the volume of solution have outflow boundary conditions. The total flow into the large volume is $3 \times 10^{-3}\, M_\odot\, \mathrm{yr}^{-1}$ with a velocity of $700\,\mathrm{km\,s^{-1}}$, a Mach number of 10, and number density of $5.5 \times 10^3\,\mathrm{cm^{-3}}$, consistent with the conditions in the Galactic Center. For all simulations, a point mass of $1 \times 10^6\, M_\odot$ is used; these simulations were initiated before the more reliable value of $2.6 \times 10^6\, M_\odot$ was known precisely (Genzel, Eckart, Ott, & Eisenhauer 1997). Also, recent work (e.g., Najarro, et al. 1997) suggests that the Galactic Center wind is dominated by a few hot stars (in particular, IRS 13E1 and 7W) with wind velocites of $\sim 1000\,\mathrm{km\,s^{-1}}$. Although these differences in mass and wind velocity should not qualitatively change our results, they will be addressed in future work.

A total of 90^3 active zones are used in the large scale simulation. The zones are geometrically scaled so that the central zones are 1/64th the size of the outermost zones. An inner boundary, one that can be thought of as a totally absorbing sphere $0.1R_A$ or 2×10^{-3} pc in radius, is used to simulate the presence of the central black hole; at every time step, the mass and internal energy density of zones in the sphere are set to small values, corresponding to a temperature of 10^4 K. Once equilibrium is reached, the hydrodynamical values of zones just outside the inner boundary are saved every ten years for 100 years, to be used as time dependent outer boundary conditions for a smaller scale simulation. The large scale simulations show that most of the wind that reaches the central $0.1 R_A$ is post-shock gas flowing in the -z direction. Figure 1 shows the radial mass accretion flux through this inner boundary versus the accretion polar angle, θ, where $\theta = 0$ corresponds to accretion along the +z axis, for a particular moment in time; the shape of the curve is not very time-dependent. The clear peak at $\theta \sim 135°$ illustrates that back-flow is dominant. That is, the flow forms a standing bowshock (or, more accurately, a compressional wave) in front of the accretor and a low density, wide-angle "Bondi tube" behind it. Figure 2 shows the total mass accretion rate through the large scale inner boundary for the 100 years that are used for the small scale simulations. The average mass accretion rate is $8.9 \pm 0.3 \times 10^{-5}\ M_\odot\ \mathrm{yr}^{-1}$, in good agreement with the estimate of $9.3 \times 10^{-5}\ M_\odot\ \mathrm{yr}^{-1}$ from Equation 1.

The small scale simulations, with 70^3 zones and a zone size scaling ratio of 1.01 (so that the outermost zones are roughly 1.4 times the size of the central zones), are 1/15th of an R_A or 1×10^{-3} pc or $1.2 \times 10^4\ R_s$ on a side. The accretion disk is simulated as a totally absorbing disk 1/50th of an R_A in radius and 3 zones ($\sim 300 R_s$) thick. One simulation has the normal to the surface of the disk pointing along the z axis (the "parallel" case) while one has the normal along the y axis (the "perpendicular" case). The large scale inner boundary results are linearly interpolated in time and trilinearly interpolated in space to produce outer boundary conditions, updated every time step, for the small scale simulations. If the large scale results dictate that a given small scale outer boundary zone does not have gas flowing into the volume of solution, that zone's boundary condition is set to outflow; during our simulations, this outflow has amounted to $< 20\%$ of the total mass inflow, which therefore represents an uncertainty of this magnitude in the final results. Note that the angular momentum in this outflow is minimal, since, as seen in Figure 1, the mass accretion flux approaches zero only along the z axis.

3.3. Results of the Hydrodynamical Simulations

The intent of the numerical simulations is to more realistically estimate the radial and azimuthal distribution of the infalling gas. The characteristics of the gaseous distribution, including the density contours and velocity vector fields at the end of the two small scale simulations, are shown in Figures 3-6.

In Paper I, it was assumed that the temperature of the infalling gas was small compared to the resulting shock temperature, T_{sh}, when the wind's kinetic energy is converted into thermal energy upon impacting the disk. That is, the gas was assumed to be highly supersonic. Figure 7 shows the averaged Mach number for the infalling wind as it impacts the disk. On average, the gas is indeed supersonic, but, particularly at moderate radii for the parallel run, individual zones reach Mach numbers as low as ~ 1.1. Due to the presence of numerical viscosity, the Mach number and the other hydrodynamical variables are variable both spatially and temporally so Figure 7 (and similar figures shown below) are only illustrative. In Figure 8 we show the temperature of the infalling wind versus radius as well as the temperature of the disk that results from converting the wind's relative kinetic energy into heat (according to Eq. 3 in Paper I with a correction factor of 1/18). The thick solid line corresponds to the perpendicular run while the thin one is from the parallel run (see Figure 9 below). Clearly, the assumption that T_{sh} is much larger than T_w, the temperature of the infalling wind, is generally but not always valid. The approximation is particularly poor for the parallel run. Note, however, that the hydrodynamical code does not include radiative cooling or relativistic corrections.

However, the assumption that the wind is in free-fall from infinity is not accurate, as Figure 9

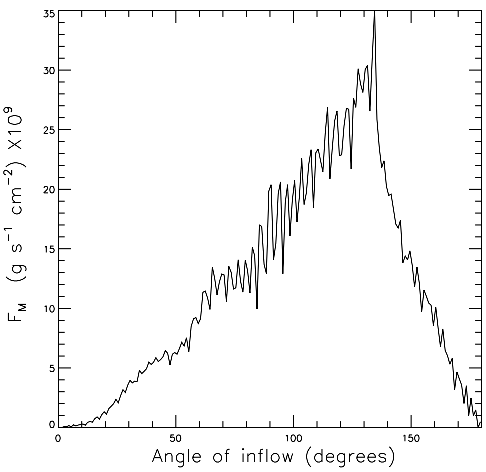

Fig. 1.— A plot of radial mass flux in $\mathrm{g\,s^{-1}\,cm^{-2}}$ versus inflow polar angle θ, summed into 1 degree bins.

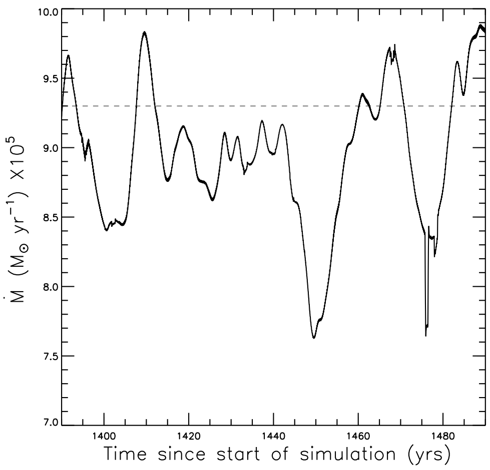

Fig. 2.— A plot of mass accretion rate (in solar masses per year) versus time since the start of the simulation (in years) for the 100 year timeslice of the large scale run that is used in the small scale simulations. Data are moving-box averaged over 40 time steps ($\sim$ 0.5 year). The dashed line is the theoretical value from Equation 1.

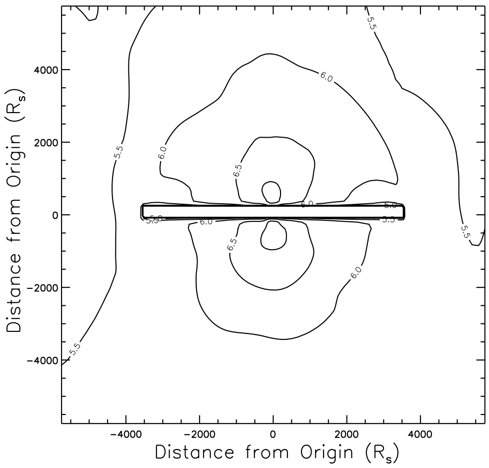

Fig. 3.— Logarithmic density contours of a slice through x=0 for the small scale parallel simulation. The large scale uniform wind originally comes from above. There are 15 contours, ranging from 10 to $10^7\,\mathrm{cm}^{-3}$. Note that the Schwarzschild radius (R_s) for a $10^6\,M_\odot$ black hole is 3×10^{11} cm.

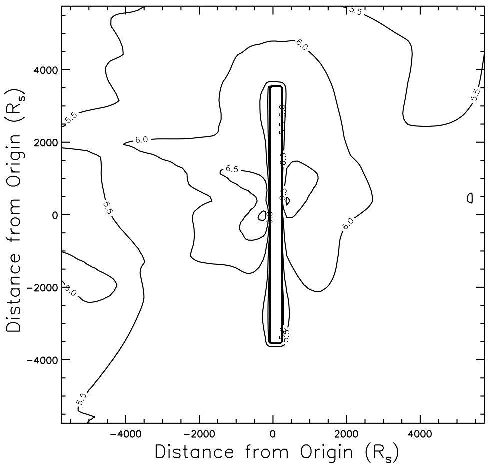

Fig. 4.— Same as Figure 3 but for the perpendicular simulation.

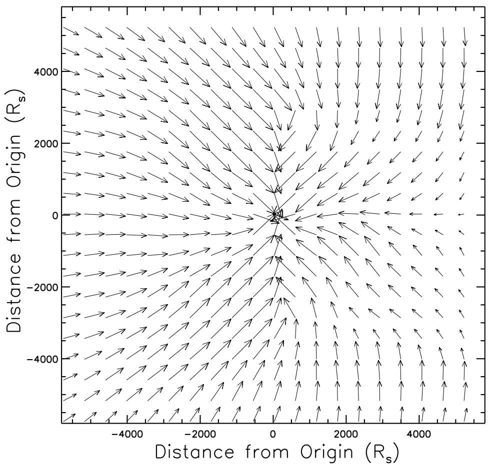

Fig. 5.— The 2 dimensional velocity vector field through x=0 for the small scale parallel simulation with the same orientation as Figure 3. Note that most of the gas is flowing in from below. The vectors are linear with the largest one corresponding to a velocity (in the x=0 plane) of $\sim 3100\,\mathrm{km\,s^{-1}}$.

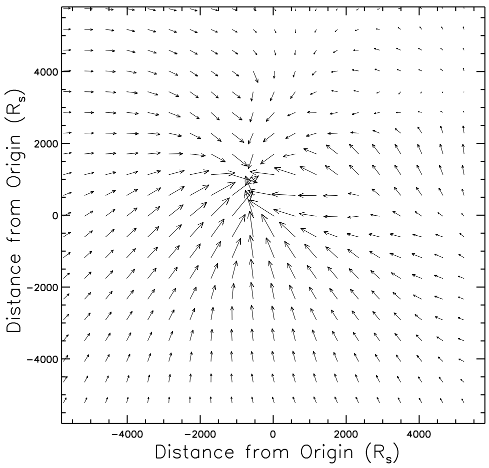

Fig. 6.— Same as Figure 5 but for the perpendicular simulation. The longest vector corresponds to a velocity (in the x=0 plane) of $\sim 8800\,\mathrm{km\,s^{-1}}$.

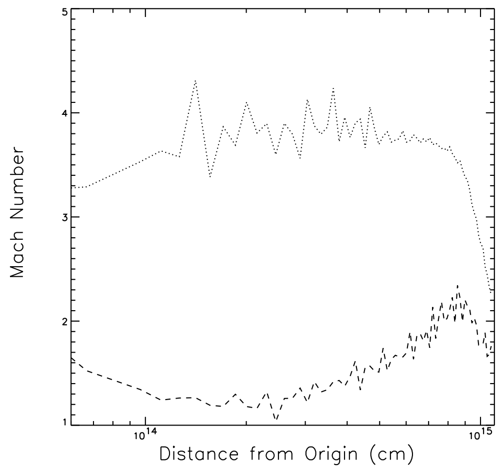

Fig. 7.— Plot of the Mach number, averaged over ϕ and the two sides of the disk, of the gas impacting the fossil disk at t = 50 years. The dotted line corresponds to the perpendicular disk simulation; the dashed line corresponds to the parallel disk simulation.

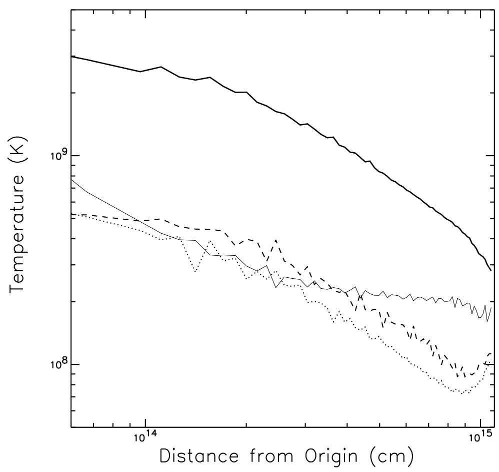

Fig. 8.— Plot of the temperature of the infalling gas right before it impacts the disk. The dotted line corresponds to the perpendicular disk simulation; the dashed line corresponds to the parallel disk simulation. The solid lines correspond to the resulting temperature for the two runs after the relative kinetic energy of the wind is converted into thermal energy. The thick solid curve is for the perpendicular run and the thin one is for the parallel run.

illustrates. The angular momentum in the wind and the obstructing presence of the disk itself cause the wind to have a non-radial profile and thus not fit the $r^{-1/2}$ free-fall expression used in Paper I. The total mass accretion rate onto the disk for both runs is $\sim 4 \times 10^{21}\,\mathrm{g\,s^{-1}}$; this is somewhat less than the total mass flow into the volume ($5.6 \times 10^{21}\,\mathrm{g\,s^{-1}}$) due to the outflow mentioned above. A plot of the resulting $\dot{\Sigma}_{\rm w}$, shown in Figure 10, is slightly flatter than a r^{-2} dependence, suggesting, as expected from Figure 1, a wind pattern that is somewhere between cylindrical and radial. That is, for a cylindrical flow, $\dot{\Sigma}_{\rm w}$ is constant with radius (in the plane), while for a radial flow intercepted by a disk of thickness $2d \ll r$,

$$r^3\,\dot{\Sigma}_{\rm w} \propto d \approx \text{constant}\ , \tag{15}$$

since $\dot{\Sigma}_{\rm w} = v_z\,\rho$, with $v_z = v_r \cos\theta$ and $\dot{M} = 4\pi\,r^2\,\rho\,v_r$.

In Figures 11 and 12 we show the mass accretion rate onto the accretion disk versus time for the parallel and perpendicular runs, respectively. A comparison with Figure 2 shows that $10-20\%$ of the gas is not falling onto the disk but rather is leaving the volume of the small scale simulation through the +z boundary. Also, note that the large scale mass accretion rate is, on the whole, temporally uncorrelated with the small scale mass accretion rate but that the accretion rate for the two runs are strongly correlated. Thus, the average rate of mass falling onto the disk is independent of the disk orientation while the velocity profile, and thus the specific angular momentum, are not. However, coincidentally, the angle between the normal of the bottom of the disk (90 or 180°) and the angle of maximum inflow (135°, see Figure 1), is 45° for both runs. A disk oriented differently with respect to the large scale inflow might result in different accretion profiles (but see section 4.3).

Similarly, Figures 13 and 14 show the specific angular momentum, λ, in units of cR_s, accreted onto the accretion disk via the wind for the parallel and perpendicular runs, respectively. In contrast to the mass accretion rate, the magnitude of λ is significantly different for the two runs, the parallel case having $\lambda = 1.6 \pm 0.2$, which is roughly 4 times lower than for the perpendicular case with $\lambda = 6.8 \pm 4.1$. The flow in the perpendicular case is considerably more turbulent, with larger temporal fluctuations in the hydrodynamical variables. It is expected that a disk with a normal along the large scale z axis would accrete less specific angular momentum since L_z is, in general, less than the other components, L_x and L_y. The two disk orientations can be thought to represent extremes of minimal and maximal capture of the specific angular momentum in the infalling wind. The effective circularization radius, where most of the wind intercepts the disk, is $\sim 4R_s$ for the parallel case and $\sim 56R_s$ for the perpendicular case. It is important to note that the specific angular momentum accreted by the disk is always less than the specific angular momentum present in the overall wind. Thus, even though recent large scale simulations (Coker & Melia 1997), involving point sources instead of a planar flow, result in larger values of λ (~ 50 at 5×10^{15} cm), any accretion disk is likely to intercept only a fraction of this because clumps with preferentially small values of λ tend to flow inwards to smaller radii.

In Figures 15-18, we present some of the velocity profiles, in cylindrical coordinates, for the wind as it falls onto the disk. For comparison, the radial velocity for a shocked gas in free-fall, corresponding to the analytical profile used in Paper I for the zero angular momentum case, is also plotted in the figures. Consistent with the small value of λ, the velocity profile for the parallel case is fairly close to the shocked free-fall profile used in Paper I while v_r for the perpendicular case is, except at small r, somewhat *faster* than the profile used in Paper I. This is a direct consequence of the non-zero velocity at infinity. In addition, the large scale bowshock is not a true shock for all angles so that a shocked free-fall profile, which is 1/4 times that of an unshocked profile, is inaccurate. Figure 19 illustrates quantitatively how the specific angular momentum present in the gas accreting onto the disk relates to that of the disk itself, which is assumed to be Keplerian so that $\lambda_d = \sqrt{GMR}$.

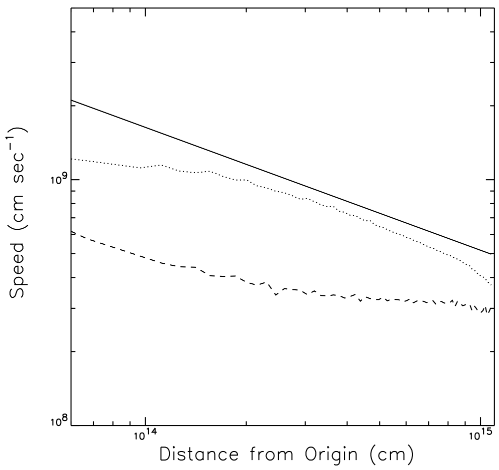

Fig. 9.— As in Figure 7, but for the speed of the gas impacting the fossil disk. The solid line corresponds to free-fall velocity from infinity.

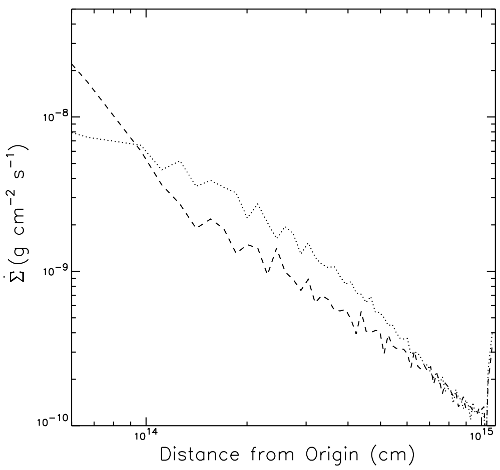

Fig. 10.— As in Figure 7, but for $\dot{\Sigma}_{\rm w}$, the total mass infall onto the disk per unit time and area.

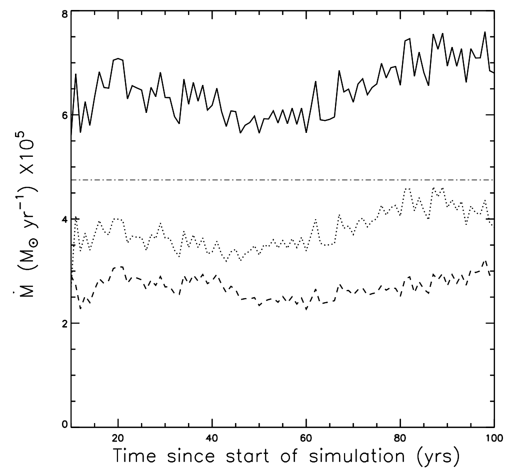

Fig. 11.— The mass accretion rate versus time onto the accretion disk due to the infalling wind for the parallel disk case. The dotted line is for the "top" side (+z) of the disk, the dashed line is for the "bottom" side, and the solid line is the sum of the two. The dot-dashed line corresponds to one half of the theoretical value from Equation 1, for direct comparison with the top and bottom rates.

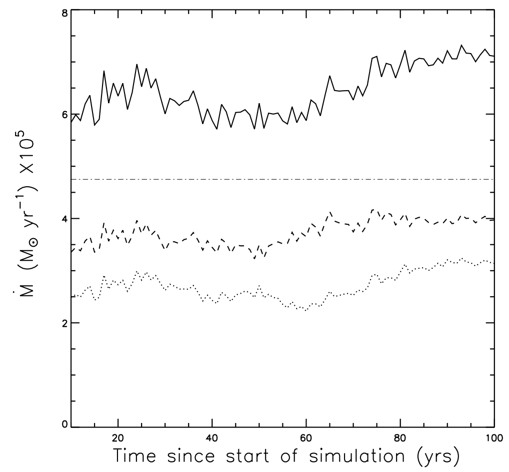

Fig. 12.— As in Figure 10, but for the perpendicular disk case.

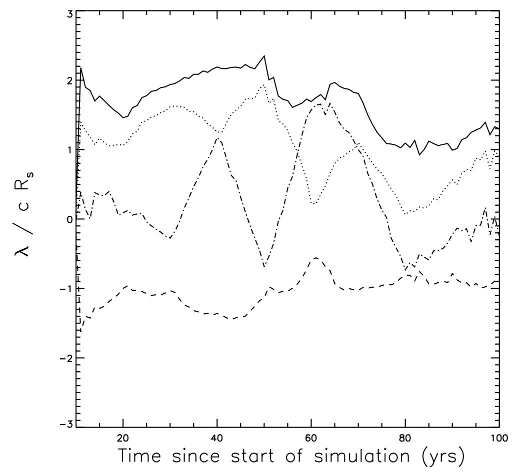

Fig. 13.— The specific angular momentum accreted by the disk versus time for the parallel case. The dotted line is λ_x, the dashed line is λ_y, and the dot-dashed line is λ_z. The solid line is the root-sum-square of the components.

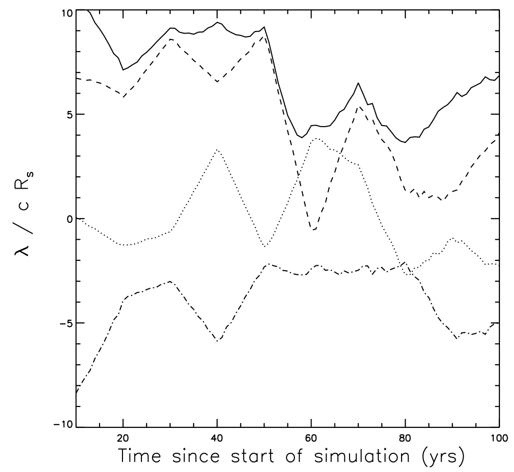

Fig. 14.— As in Figure 12, but for the perpendicular disk case. Note that for this plot, $\hat{z}$ is parallel to the normal to the disk surface, corresponding to the large scale y axis.

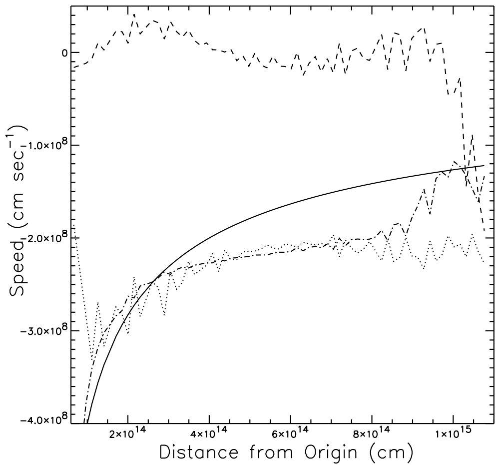

Fig. 15.— The velocity profile for gas falling onto the "top" side of the disk for the parallel run at t = 50 years. The dotted line is v_r, the dashed line is v_ϕ, and the dot-dashed line is v_z. The solid line is the $r^{-1/2}$ profile of a shocked free-falling gas (which is 1/4 the velocity of a gas free-falling from infinity).

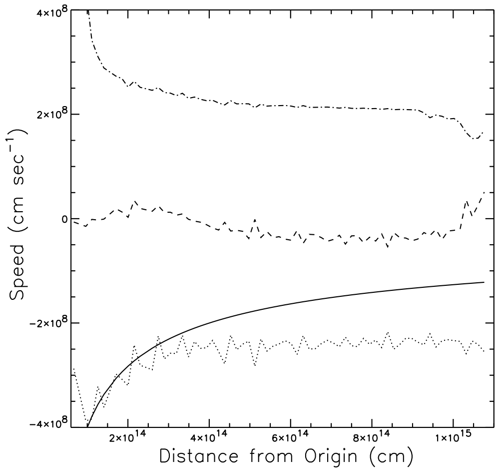

Fig. 16.— As in Figure 15, but for the "bottom" side of the disk.

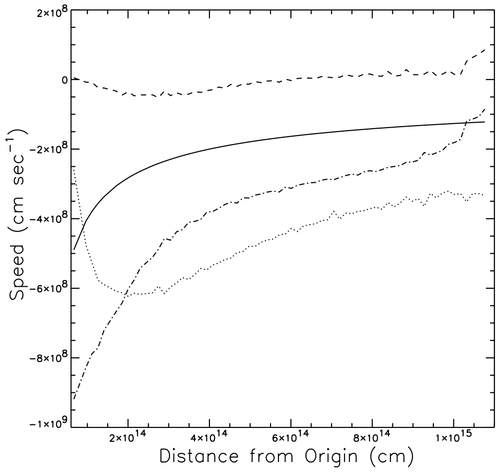

Fig. 17.— As in Figure 15, but for the perpendicular run. Note that for this plot, $\hat{z}$ is parallel to the normal to the disk surface.

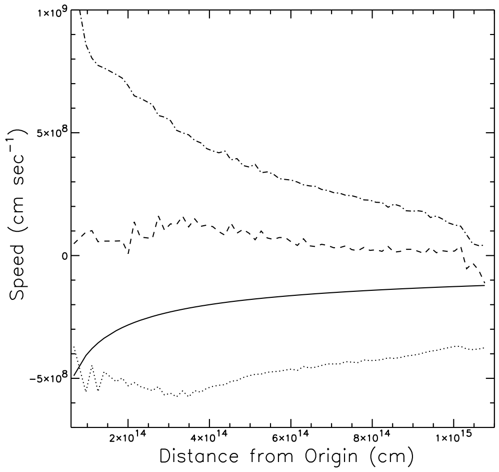

Fig. 18.— As in Figure 17 but for the “bottom” side of the disk. For this plot, $\hat{z}$ is parallel to the normal to the disk surface.

For the purpose of using the 3D hydrodynamical results for the quasi-analytical disk evolution calculations below, we have averaged the flow variables over ϕ. However, due to the asymmetric and time-dependent outer boundary conditions, the flow has azimuthal structure. Figures 20-23 show where the specific angular momentum is deposited on the disk. The lack of symmetry is particularly evident near the edge of the disk, where its absorbing boundary induces instabilities in the inflow. More specific angular momentum is deposited in the central region for the perpendicular calculation, consistent with the larger average value of λ in this case. Although the magnitude of the fluctuations in λ, both spatially and temporally, are sometimes large (for example, note the difference between Figures 22 and 23), the time scale for these variations is short compared with the disk evolution time scale (see below) and these variations are therefore not likely to affect our conclusions.

3.4. Power-law Fitting

As evidenced by the preceeding plots, a power-law fit to the velocity profiles is not always accurate. However, for our purposes, a simple power-law allows for easy evolution of the disk equations. In any case, our final results are not overly sensitive to the precise exponents for $\dot{\Sigma}_{\rm w}$ $v_{\rm r}$, and $v_{\rm z}$.

The 3D hydrodynamical data are first averaged over ϕ and then put into radial bins of 50 R$_s$. This bin size was chosen so as to give some idea of the magnitude of the fluctuations of the hydrodynamical variables while still showing the large scale trends. The volume of each zone was used as a weight when averaging. A given zone was used in calculating results for the top or bottom side of the disk, depending on the sign of v_z. These values were used in making the previous plots.

Next, a linear least squares fit was applied to the binned and averaged data from years 50-99. The results of these fits were then averaged to get our final power-laws for $\dot{\Sigma}_{\rm w}$ $v_{\rm r}$, and $v_{\rm z}$. For the perpendicular case we get:

$$\begin{aligned}
\dot{\Sigma}_{\rm w}(r) &= 1.35 \cdot 10^{17} \text{ g/cm}^2 \, (r/\text{cm})^{-1.8} & (16)\\
v_{\rm r}(r) &= 2.19 \cdot 10^{12} \text{ cm/sec} \, (r/\text{cm})^{-0.25} & (17)\\
v_{\rm z}(r) &= 8.51 \cdot 10^{18} \text{ cm/sec} \, (r/\text{cm})^{-0.71} & (18)\\
R_{circ} &= 56 R_s \, , & (19)
\end{aligned}$$

while for the parallel case we get:

$$\begin{aligned}
\dot{\Sigma}_{\rm w}(r) &= 1.17 \cdot 10^{11} \text{ g/cm}^2 \, (r/\text{cm})^{-1.39} + 1.07 \cdot 10^{17} \text{ g/cm}^2 \, (r/\text{cm})^{-1.8} & (20)\\
v_{\rm r}(r) &= 1.35 \cdot 10^{10} \text{ cm/sec} \, (r/\text{cm})^{-0.12} & (21)\\
v_{\rm z}(r) &= 1.62 \cdot 10^{13} \text{ cm/sec} \, (r/\text{cm})^{-0.33} & (22)\\
R_{circ} &= 4 R_s \, . & (23)
\end{aligned}$$

The velocity profile is the average of the results for the top and bottom of the disk while $\dot{\Sigma}_{\rm w}$ is the sum. R_{circ} is the circularization radius (given by $2\lambda^2$) determined from the time averaged value of λ. As expected from the small values of λ, the azimuthal velocity, v_ϕ, is always smaller than v_r and v_z and is, on average, zero. Note that Equation 20 has two components, one from each side of the disk. The flatter term arises from the bottom side of the disk. This is a result of the entire "Bondi tube" impacting the bottom of the disk at relatively large radii; in the perpendicular case, it impacts both sides of the disk. This is also the reason for the flatter velocity profiles in the parallel case.

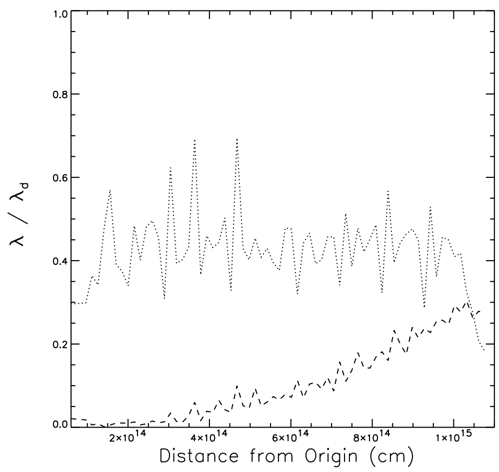

Fig. 19.— Plot of λ/λ_d, averaged over ϕ and the two sides of the disk, at t = 50 years. The dotted line corresponds to the perpendicular disk simulation; the dashed line corresponds to the parallel disk simulation.

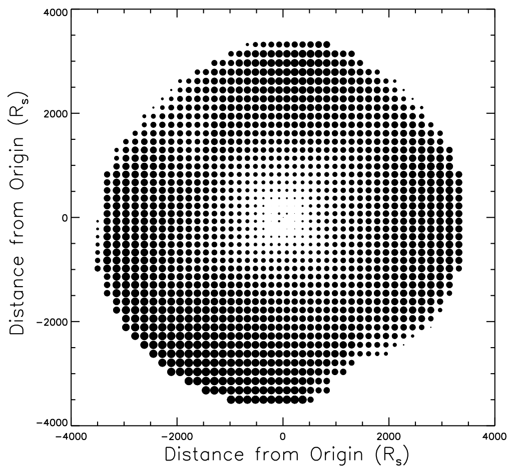

Fig. 20.— A graphical representation of the specific angular momentum deposited on the top side of the disk by the infalling wind for the parallel calculation. The diameter of the black circles is proportional to the logarithmic value of λ; circles that are just touching correspond to $\lambda \approx 10$.

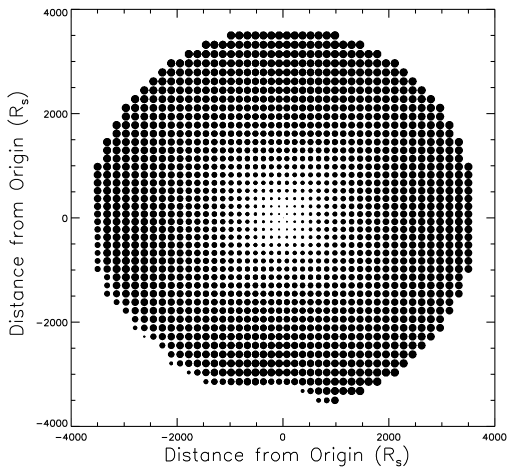

Fig. 21.— As in Figure 20 but for the specific angular momentum deposited on the bottom side of the disk for the parallel calculation.

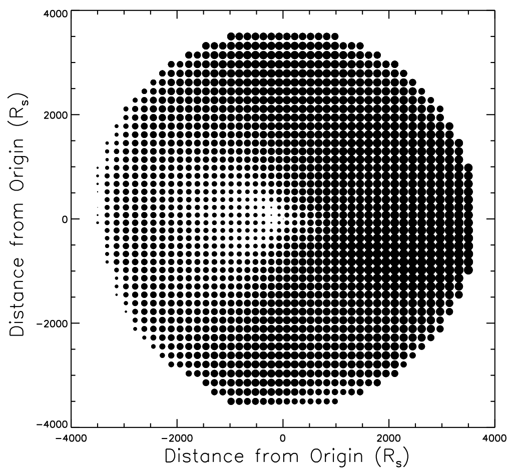

Fig. 22.— As in Figure 20 but for the specific angular momentum deposited on the top side of the disk for the perpendicular calculation.

4. The Disk Evolution with a Hydrodynamic Wind Infall

We can now use the results of the 3D hydrodynamical calculations to determine the temporal evolution of an accretion disk subject to a wind infall. Here we will be using the 1D accretion disk code described in Falcke & Melia (1997). The code traces the evolution of a standard accretion disk with infall according to the Equations of section 2, which are employed with an arbitrary radial mass deposit as input. A major problem in combining the 3D wind simulations with the 1D accretion disk calculations is that the length and time scales are vastly different between the two. The 3D simulations do not have sufficient resolution to model the infall at small radii. Moreover, they span only a period of a few hundred years. On the other hand, the disk evolves on a scale of 10^{4-5} years. In addition, the disk code can neither take into account azimuthal asymmetries of the inflow, nor properly handle the differences in infall between the top and bottom sides of the disk. One therefore has to make a number of simplifying assumptions.

We said earlier how one can roughly approximate the basic parameters of the inflow as power-laws, e.g., for $\dot{\Sigma}_{\rm w}$ $v_{\rm r}$, and $v_{\rm z}$. For $\dot{\Sigma}_{\rm w}$, the input for the disk simulations will then be the sum of top and bottom sides, while for $v_{\rm z}$ we take the average. The internal energy of the wind in our 3D simulations is generally small compared to its kinetic energy and will be neglected. We then have to assume that these power-laws remain constant over the typical disk evolution time scale. We also need to assume that the power-laws can be extrapolated down to the circularization radius. For numerical reasons, we also truncate the wind infall at 10^{15}cm, and allow the actual accretion disk to extend outwards to three times this distance.

The functional forms of $\dot{\Sigma}_{\rm w}$ yield a wind infall rate of approximately $10^{-4}M_{\odot}/{\rm yr}$. The inner wind radius is given by the circularization radius. The accretion disk evolution always begins with the adoption of a Shakura-Sunyaev configuration with $\alpha = 10^{-4}$, $\dot{M} = 10^{-6}M_{\odot}/{\rm yr}$, and a central mass $M_{\bullet} = 10^{6}M_{\odot}$, consistent with the 3D hydrodynamical simulation. Following Falcke & Melia (1997), we calculate the disk's spectrum by integrating local blackbodies. We note that in the parallel case the top and bottom sides receive different mass depositions from the wind and hence are subjected to different energy dissipation rates. As such, the actual spectra of the top and bottom sides will generally not be the same. Given our computational limitations and the fact that the modest difference will not significantly change our conclusions, we are going to ignore this effect in the following.

The results of our calculations are shown in Figures 24-27 for the perpendicular case and in Figures 28-31 for the parallel case. Many of the results of our disk calculations that incorporate the 3D hydrodynamical simulations can be understood in terms of the various possibilities outlined in our previous paper (Falcke & Melia 1997), but several interesting new features are now apparent, and we discuss these in the next section.

4.1. The Perpendicular Case

At large radii, the wind infall dominates the accretion rate. The infall rate, which is proportional to $\dot{\Sigma}_{\rm w}r^2$, is roughly constant between the circularization radius and the outermost radius of the wind. This implies an $\dot{M}$ that increases linearly inwards with r in the disk. In addition, however, the low angular momentum of the wind will act as a brake to the disk's rotation and therefore speed-up the radial accretion in the disk. Inside the circularization radius, where the wind impact is negligible, the increased mass accretion rate has to be transported by viscous processes and hence the solution will become more Shakura-Sunyaev like again. Once the disk has developed towards an equilibrium state the accretion rate in the disk (Fig. 24) will increase as a power-law throughout the wind region and become constant inside

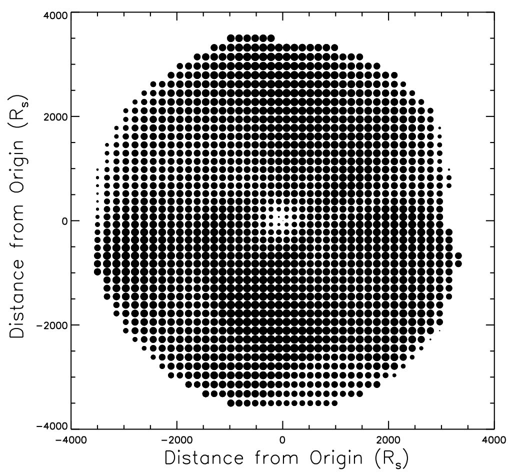

Fig. 23.— As in Figure 20 but for the specific angular momentum deposited on the bottom side of the disk for the perpendicular calculation.

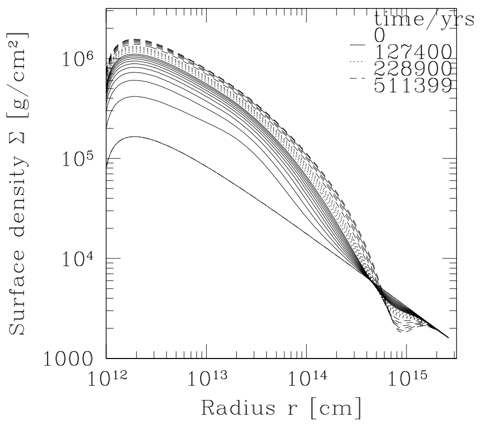

Fig. 24.— Evolution of the surface density of an accretion disk with wind infall when the incoming ambient flow is perpendicular to the disk's rotation axis. The disk is a standard α-disk with $\alpha = 10^{-4}$ and $\dot{M} = 10^{-6} M_{\odot}/\mathrm{yr}$ around a black hole of $10^6 M_{\odot}$. Different lines correspond to different time steps (equidistant for equal line styles) as shown in the legend. The initial Shakura-Sunyaev solution coincides with the first solid line.

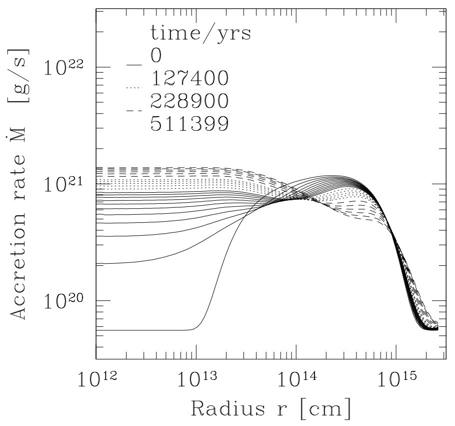

Fig. 25.— Same as Figure 24, but here the local accretion rate in the disk is shown.

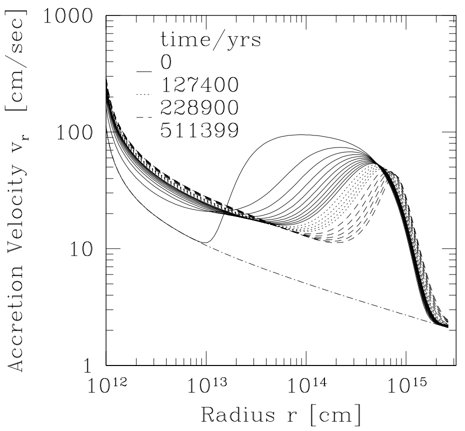

Fig. 26.— Same as Figure 24, but here the radial accretion rate velocity in the disk is shown. The initial Shakura-Sunyaev solution is given as the dashed-dotted line.

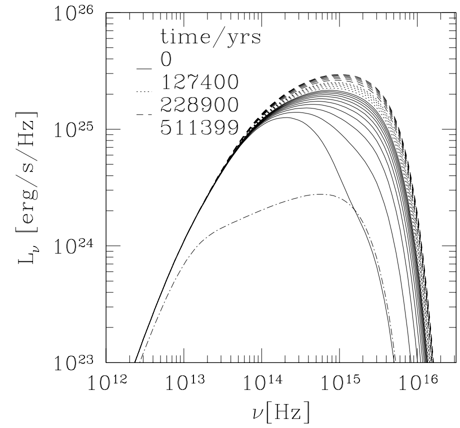

Fig. 27.— The disk spectrum for the case shown in Figure 24. The initial Shakura-Sunyaev solution corresponds to the dashed-dotted line.

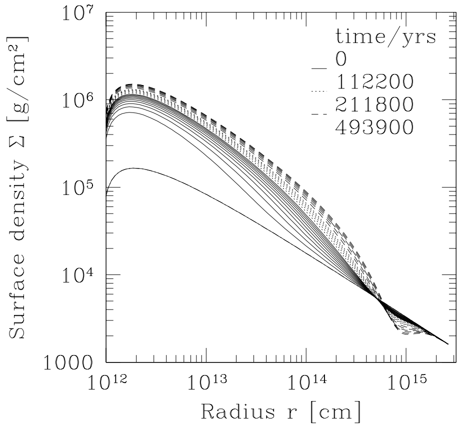

Fig. 28.— Evolution of the surface density of an accretion disk with wind infall when the direction of the ambient flow is parallel to the disk's rotation axis. The disk is a standard α-disk with $\alpha = 10^{-4}$ and $\dot{M} = 10^{-6} M_\odot/\mathrm{yr}$ around a black hole with mass $10^6 M_\odot$. Different lines correspond to different time steps (equidistant for equal line styles) as shown in the legend.

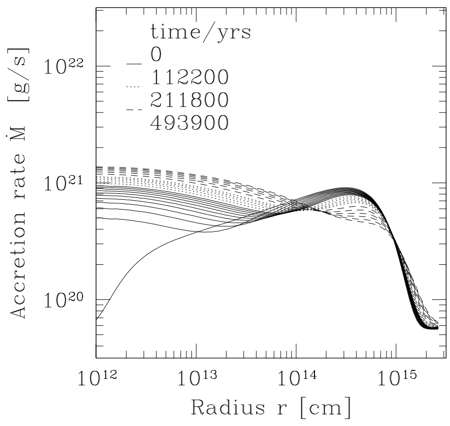

Fig. 29.— Same as Figure 28, but here the local accretion rate in the disk is shown.

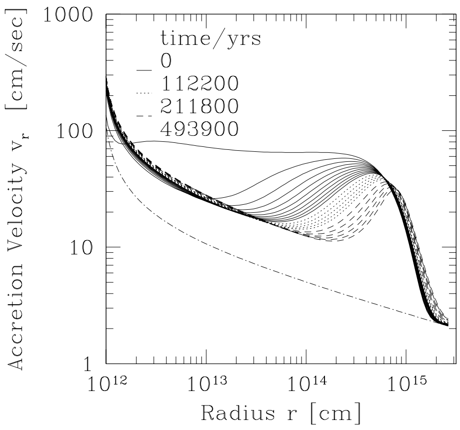

Fig. 30.— Same as Figure 28, but here the radial accretion velocity in the disk is shown.

the circularization radius.The radial velocity changes in a commensurate way.

The effect on the radiated spectrum is predictable: the impact of the low-angular momentum wind on the fossil disk leads to an immediate release of energy at large radii where most of the mass is deposited. This is reflected by the presence of a strong NIR/IR-bump in the spectrum. Only after a period of a few times 10^5 years do the viscous processes begin to transport the increased mass deposition inwards, leading to a corresponding rise in the spectrum at higher frequencies. The exact location of the NIR/IR-bump will depend on the size of the fossil disk. A larger disk will produce a bump at somewhat lower frequencies and require accordingly a longer time scale to evolve.

4.2. The Parallel Case

A slightly different behavior is evident when the ambient flow is parallel to the disk axis. The radial dependence of $\dot{\Sigma}_{\rm w}$ has a steep component (from the top side) like in the perpendicular case, which, however, has a very small circularization radius. This means that a significant amount of mass is deposited relatively close in. Moreover, on the bottom side of the disk, most of the mass is still being deposited at large radii. Consequently, the whole disk, and not only the outer part, is forced to react to the infalling wind immediately, and initially $\dot{M}$ will be high at all radii. This increase of $\dot{M}$ at small radii will lead to an increased radiation at higher frequencies, while the impacting wind at larger radii will produce a strong IR/NIR-bump. Since the dissipation of energy in the wind impact zone is basically happening on a very short time scale (disk height divided by free-fall velocity), the effect on the low-frequency part of the spectrum is still more pronounced. Only after a viscous timescale, when equilibrium is re-established and the increased mass inflow at large radii is transported through the disk to the smallest radii, will the spectrum become dominated by the hot, innermost part of the disk.

4.3. Precession and Disruption

A serious limitation of our calculations is that the disk orientation is fixed in space. However, as we have shown earlier, the impact of the wind in the parallel case is different on the top and bottom sides of the disk, and at different azimuths. One may therefore reasonably expect that this gradient in wind pressure can lead to a (differential) precession of the disk and possibly also to an eventual re-orientation of its symmetry axis or to its overall disruption. While a disruption would require a fairly sophisticated treatment, taking into account all possible instabilities, a change in the rotation axis can be dealt with in a simple, though crude, way.

Since the most symmetric accretion profile of the infalling gas appears to be associated with the perpendicular case, where the ram pressure of the wind is most evenly distributed, one can expect that an otherwise oriented disk would tend to evolve towards this state. We also can expect that a change of the disk's orientation will have occurred by the time the accumulated mass has exceeded the initial mass in the disk. Interestingly, for the parameters chosen here, the mass in the inner 10^{13} cm of the disk is only $10^{-2}M_{\odot}$, so that the inner fossil disk in the parallel case will be overwhelmed after only a few hundred years, while for the outer part of the disk (at 10^{15} cm) the corresponding time is some 10^4 years. Consequently for the type of disk used here, the parallel configuration will probably never reach a stationary solution and it will either be disrupted early or it will evolve towards the perpendicular case. Again, this behaviour will depend very critically on the initial disk conditions. Decreasing α even further will increase the disk mass and decrease the relative influence of the wind. Alternatively, a larger disk would, at least in its outer parts, be much more stable, e.g., if the fossil disk would extend to 10^{17}cm (in which case $M_{\rm disk} \simeq 10^3 M_\odot$), the time scale for disruption would then increase to more than 10^7 years.

5. Conclusions and Possible Applications

The 3D hydrodynamical calculations used here show that the usual assumption of a hypersonic free-falling wind is not always accurate. The presence of multiple wind sources, the gas conditions at infinity, the orientation of the fossil disk, and the thermal pressure of the gas all serve to modify the velocity profile of the accreting wind.

The wind infall onto the disk can in principle deposit mass at a rate anywhere between $\dot\Sigma_{\rm w}$ = constant and $\dot\Sigma_{\rm w} \propto r^{-3}$. The former results from a relatively uniform, cylindrical flow onto the disk, whereas the latter limit occurs when the inflow is purely radial. At least for the two cases considered here, the actual calculated rate ($\sim r^{-1.8}$) was somewhat closer to the second possibility than the first, implying that even though the plasma velocity configuration at large radii may be uniform, the inflow becomes more radial at small radii where it merges onto the disk. The net effect of this is that $\dot M$ through the disk then increases roughly linearly with inverse radius, and the observational impact of a wind infall is then felt on a relatively short time scale (i.e., hundreds of years) compared to the viscous time scale of a fossilized disk. We have also considered the likely effect on the disk's stability due to this infall, and based on our results, we concluded that a disk will probably rotate in time until its symmetry axis is perpendicular to the incoming wind flow direction.

An additional rather robust result of our simulations is that the emitted spectrum of a wind-fed disk can be observationally distinct from that of a pure Shakura-Sunyaev flow. Depending on where most of the wind deposition occurs, the ensuing dissipation of the wind's kinetic energy at the disk's surface contributes a significant fraction of the overall infrared luminosity. For example, in Figure 31, not only is the flux higher by an order of magnitude compared to that of the Shakura-Sunyaev solution, but more importantly as an observational diagnostic, the spectrum at infrared frequencies is steeper than in the Shakura-Sunyaev case. This feature is relatively independent of any particular application and so it is likely to be common in any wind-fed disk system.

We have considered the possibility that Sgr A* may be surrounded by a fossil disk accreting at a rate of $10^{-6} M_\odot/{\rm yr}^{-1}$, while intercepting an infalling wind of $10^{-4} M_\odot/{\rm yr}^{-1}$. Current infrared observational limits for Sgr A* are very restrictive, with $L_\nu \lesssim 10^{21}$ ergs sec^{-1}Hz^{-1} at 10^{14} Hz. We have found that, for the wind configuration we have considered here, the predicted infrared luminosity is more than 3 orders of magnitude greater than the observational limits. It seems likely that even if the gas circularizes at a large radius ($\gtrsim 10^{16}$ cm or $\lambda \gtrsim 100$) and has an extremely low viscosity ($\alpha \lesssim 10^{-4}$), the observational limits will be violated. In any case, hydrodynamical simulations (Coker & Melia 1997) suggest that, even including more realistic individual point sources, the value of λ is probably $\lesssim 50$. Thus it seems unlikely that a standard massive fossilized disk may be present around Sgr A*.

Many of these conclusions apply also to other types of disks, such as an advection dominated one. However, the equations we have used in this paper to describe the disk evolution cannot adequately handle the internal structure of such a configuration, and we must await future developments employing the proper global equations in order to make conclusive statements involving the fate of these disks when they intercept a rather strong Bondi-Hoyle inflow. The state variables depend on the gradients of quantities such as the temperature, as well as their local values. Nonetheless, it is safe to conclude that the kinetic energy dissipated above the disk by the infalling wind is likely to produce a spectral signature that is inconsistent with the observations for any type of large scale disk.

Thus, based on our application to the Galactic center source, Sgr A*, our results would seem to argue against there being any type of large scale disk (i.e., with radius $\gg 50r_g$) feeding the central mass concentration, and that instead the inflow into this object probably swirls toward small radii without ever forming a stable, flattened configuration.

Acknowledgments This research was partially supported by NASA under grant NAGW-2518.

REFERENCES

Abramowicz, M.A., Chen, X., Kato, S., Lasota, J. P., & Regev, O. 1995, *ApJ (Letters)*, **438**, L37.

Allen, D., Hyland, A., & Hillier, D. 1990, *MNRAS*, **244**, 706.

Backer, D. 1996, in IAU Symp. 169, Unsolved Problems of the Milky Way, ed. L. Blitz & Teuben P.J. (Dordrecht: Kluwer), XXX

Beckert, T., Duschl, W., Mezger, P., & Zylka R. 1996, A&A, **307**, 450.

Bondi, H, & Hoyle, F. 1944, *MNRAS*, **104**, 273.

Coker, R. & Melia, F. 1996, in ASP Conf. Vol. 102, The Galactic Center: 4th ESO/CTIO Workshop, ed. R. Gredel (San Francisco: ASP), 403.

Coker, R. & Melia, F. 1997, *ApJ (Letters)*, **488**, L149.

Duschl, W. 1989, *MNRAS*, **240**, 219.

Eckart, A. & Genzel, R. 1997, *MNRAS*, **284**, 576.

Falcke, H. 1996, in IAU Symp. 169, Unsolved Problems of the

Falcke, H. & Biermann, P.L. 1999, A&A, **342**, 49. Milky Way, ed. L. Blitz & Teuben P.J. (Dordrecht: Kluwer), 163

Falcke, H. & Melia, F. 1997, *ApJ*, **479**, 740.

Falcke, H. & Heinrich, O. 1994, A&A, **292**, 430.

Falcke, H., Mannheim, K., & Biermann, P. L. 1993, A&A, **278**, L1.

Gatley, I., Jones, T., Hyland, A., Wade, R., Geballe, T., & Krisciunas, K. 1986, *MNRAS*, **222**, 299.

Geballe, T., Krisciunas, K., Bailey, J., & Wade, R. 1991, *ApJ (Letters)*, **370**, L73.

Genzel, R., Eckart, A., Ott, T., & Eisenhauer, F. 1997, *MNRAS*, **291**, 219.

Hall, D., Kleinmann, S., & Scoville, N. 1982, *ApJ (Letters)*, **260**, L53.

Haller, J.W., Rieke, M.J., Rieke, G.H., Tamblyn, P., Close, L., & Melia, F. 1995, *ApJ*, **456**, 194.

Khokhlov, A.M. & Melia, F. 1996, *ApJ (Letters)*, **457**, L61.

Krabbe, A., Genzel, R., Drapatz, S., & Rotaciuc, V. 1991, *ApJ (Letters)*, **382**, L19.

Krabbe, A., Genzel, R., Eckart, A. et al. 1995, *ApJ (Letters)*, **447**, L95.

Lacy, J., Achtermann, J., & Serabyn, E. 1991, *ApJ (Letters)*, **380**, L71.

Melia, F. 1992, *ApJ (Letters)*, **387**, L25.

Melia, F. 1994, *ApJ*, **426**, 577.

Melia, F. 1996, in ASP Conf. Vol. 102, The Galactic Center: 4th ESO/CTIO Workshop, ed. R. Gredel (San Francisco: ASP), 395.

Melia, F., Coker, R. F., & Yusef-Zadeh, F. 1996, *ApJ (Letters)*, **460**, L33.

Melia, F., Jokipii, R., & Narayanan, A. 1991, *ApJ (Letters)*, **395**, L87.

Menten, K., Reid, M., Eckart, A., & Genzel, R. 1997, *ApJ (Letters)*, **475**, L111.

Najarro, F., Hillier, D., Kudritzki, R., Krabbe, A., Genzel, R., Lutz, D., Drapatz, S., & Geballe, T. 1994, A&A, **285**, 573.

Najarro, F., Krabbe, A., Genzel, R., Lutz, D., Kudritzki, R., & Hillier, D. 1997, A&A, **325**, 700.

Narayan, R., Yi, I., & Mahadevan, R. 1995, *Nature*, **374**, 623.

Norman, M. 1994, BAAS, 184, 50.01

Petrich, L., Shapiro, S., Stark, R., & Teukolsky, S. 1989, *ApJ*, **336**, 313.

Predehl, P. & Trümper, J. 1994, A&A *(Letters)*, **290**, L29.

Ruffert, M. 1996, A&A, **311**, 817.

Ruffert, M. & Anzer, U. 1995, A&A, **295**, 108.

Ruffert, M. & Melia, F. 1994, A&A *(Letters)*, **288**, L29.

Stone, J.M. & Norman, M.L. 1992, ApJS, 80, 753

Yusef-Zadeh, F. & Melia, F. 1991, *ApJ (Letters)*, **385**, L41.

Yusef-Zadeh, F. & Wardle, M. 1993, *ApJ*, **405**, 584.

Zylka, R., Mezger, P.G., Ward-Thomson, D., Duschl, W., & Lesch, H. 1995, A&A, **297**, 83.

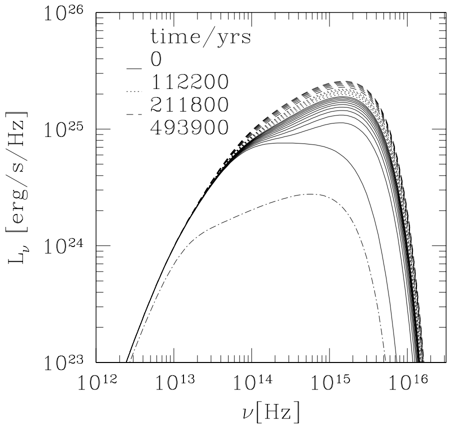

Fig. 31.— The emitted spectrum corresponding to the case shown in Figure 28.